Study on a Quaternary Working Pair of CaCl₂-LiNO₃-KNO₃/H₂O for an Absorption Refrigeration Cycle

Yiqun Li [1], Na Li [2], Chunhuan Luo [1,3] and Qingquan Su [1,3,*]

[1] School of Energy and Environmental Engineering, University of Science and Technology Beijing, Beijing 100083, China; liyiqun1616@gmail.com (Y.L.); luochunhuan@ustb.edu.cn (C.L.)

[2] State Grid Energy Conservation Service CO., Ltd., Beijing 100083, China; b20150273@xs.ustb.edu.cn

[3] Beijing Higher Institution Engineering Research Center of Energy Conservation and Environmental Protection, University of Science and Technology Beijing, Beijing 100083, China

* Correspondence: suqingquan@ustb.edu.cn

Abstract: When compared with LiBr/H₂O, an absorption refrigeration cycle using CaCl₂/H₂O as the working pair needs a lower driving heat source temperature, that is, CaCl₂/H₂O has a better refrigeration characteristic. However, the crystallization temperature of CaCl₂/H₂O solution is too high and its absorption ability is not high enough to achieve an evaporation temperature of 5 °C or lower. CaCl₂-LiNO₃-KNO₃(15.5:5:1)/H₂O was proposed and its crystallization temperature, saturated vapor pressure, density, viscosity, specific heat capacity, specific entropy, and specific enthalpy were measured to retain the refrigeration characteristic of CaCl₂/H₂O and solve its problems. Under the same conditions, the generation temperature for an absorption refrigeration cycle with CaCl₂-LiNO₃-KNO₃(15.5:5:1)/H₂O was 7.0 °C lower than that with LiBr/H₂O. Moreover, the cycle's COP and exergy efficiency with CaCl₂-LiNO₃-KNO₃(15.5:5:1)/H₂O were approximately 0.04 and 0.06 higher than those with LiBr/H₂O, respectively. The corrosion rates of carbon steel and copper for the proposed working pair were 14.31 μm·y⁻¹ and 2.04 μm·y⁻¹ at 80 °C and pH 9.7, respectively, which were low enough for engineering applications.

Keywords: absorption refrigeration; working pair; crystallization temperature; vapor pressure; COP; corrosivity

1. Introduction

Absorption refrigeration systems can effectively utilize not only industrial waste heat [1–4], but also low-grade renewable energy, including solar energy and geothermal energy for refrigeration [5–7]. As a traditional working pair, LiBr/H₂O has been widely used for refrigeration [8–12]. However, studies on new working pairs are still ongoing, because the required temperature of driving heat source for a refrigeration cycle using LiBr/H₂O even reaches 88.0 °C [13–15], which is too high to use for some low-grade heat sources. Lin et al. [16] studied a double-stage air-cooled NH₃/H₂O absorption refrigeration system and found that it could effectively lower the temperature of driving heat source for utilizing solar energy. Malinina et al. [17] analyzed the influences of temperature and humidity on a solar energy refrigeration system with LiBr/H₂O and calculated the minimum heat-collecting temperatures that are based on solar energy in some cities. Mortazavi et al. [18] designed an absorption refrigeration system with a falling-film generator, which could use lower temperature waste heat or solar energy. Bourouis et al. [19] analyzed the performance of LiBr + LiNO₃ + LiCl + LiI + H₂O in a vertical tube and found that the crystallization temperature was 35 °C lower than LiBr solution. Sun et al. [20] studied LiBr-LiNO₃ (mole ratio: 4:1)/H₂O and found the alternative working pair had higher COP and

less corrisivity than LiBr/H$_2$O. Chen et al. [21] studied the performance of an absorption refrigeration system using [emim]Cu$_2$Cl$_5$/NH$_3$ as working pair with the UNIFAC model, and results showed that the [emim]Cu$_2$Cl$_5$/NH$_3$ system possessed several advantages, including non-crystallization and non-corrosion. Bellos et al. [22] compared the exergy efficiency between LiCl/H$_2$O and LiBr/H$_2$O, results showed that LiCl/H$_2$O performed better at different ambient temperature levels. Wang et al. [23] measured the properties of different ammonia/ionic liquid working pairs. Luo et al. [24–28] studied various lithium nitrate-ionic liquid/water working pairs. They both found that the working pairs with ionic liquid had excellent characteristics for heating, whereas they were not suitable for refrigeration because of insufficient absorption ability. Li et al. [29–32] measured the thermophysical properties of several CaCl$_2$-based working pairs, and found that the CaCl$_2$-based working pairs had an excellent refrigeration characteristic. However, their strong corrosivity limited the practical applications.

In this work, to find a new working pair with excellent refrigeration characteristic for absorption refrigeration, various inorganic salts, including NaCl, KCl, LiCl, KNO$_3$, and LiNO$_3$, were added in CaCl$_2$/H$_2$O, and their crystallization temperature and saturated vapor pressure were measured. Furthermore, some other thermophysical properties and corrisivity of the proposed working pair were measured and the performance of an absorption refrigeration cycle with the proposed working pair was analyzed.

2. Experiments

2.1. Materials

Table 1 shows the purities of the reagents used in this work. Table 2 lists the detailed compositions of carbon steel and copper samples used in the corrosion experiments.

Table 1. Purity of the used regents.

Reagent	Mass Concentration Purity	Provenance
CaCl$_2$	>0.96	Sinopharm Chemical Reagent Beijing
NaCl	>0.995	Sinopharm Chemical Reagent Beijing
KNO$_3$	>0.99	Sinopharm Chemical Reagent Beijing
KCl	>0.995	Sinopharm Chemical Reagent Beijing
LiCl	>0.95	Tianjin Jinke Chemical
LiNO$_3$	>0.995	Tianjin Jinke Chemical
Ultrapure water		Home-made

Table 2. Chemical compositions of carbon steel and copper.

Component	C	Mn	Si	P	S	Zn	Pb	Sn	Fe	Cu
Carbon steel Q235	0.16	0.53	0.3	0.035	0.04	–	–	–	balance	–
Copper T6	–	–	0.006	–	0.01	0.005	0.05	0.05	0.05	balance

2.2. Apparatus and Methods

To analyze the performance of a working pair, its properties, such as crystallization temperature, saturated vapor pressure, density, viscosity, specific heat capacity, dissolution enthalpy, and corrosion rate, need to be measured.

The crystallization temperature was measured by a dynamic method in a precision thermostat (HX-3010, Bilang, Shanghai). The prepared solution was put in the thermostat at a slightly higher initial temperature. The crystallization temperature was measured by reducing the temperature by 1 °C every 12 hours until crystallization appeared in the solution.

The saturated vapor pressure was measured by a static method. The solution was poured into an autoclave that was assembled with a precision digital absolute pressure gauge (AX-110, Aoxin, Xi'an) and a Pt-100 thermocouple. The autoclave was placed in a precision oil bath (DKU-30, Jinghong,

Shanghai) after vacuuming. The data of pressure gauge and thermocouple were obtained, respectively, after stabilization.

The density and viscosity were measured in a precision viscometer oil bath (SYP1003-H, Zhongxi, Beijing). Density measurement was carried out by a capillary pycnometer with a capillary diameter of approximately 1 mm. Ubbelohde capillary viscometers with different fine capillaries was used to carry out the viscosity measurement.

The specific heat capacity and dissolution enthalpy were measured by a micro reaction calorimeter (μRC, THT Co., UK). The measurement of specific heat capacity was conducted by making a 1 °C "step-change" in the measurement temperature. The dissolution enthalpy was measured by an isothermal method, with a solid addition accessory.

The corrosion rate of carbon steel and copper in the solution were measured by a weight loss method. The sample was immerged in the solution for 200 hours. The corrosion rate was calculated according to the mass change of the sample.

References [24–28] give the detailed procedures. All the above experiments were carried out at 101.3 kPa and 25 °C. The properties of water and $LiBr/H_2O$ were measured and compared with literature values to validate the above methods. In addition, three parallel experiments were carried out for each measurement to verify the reproducibility. Table 3 lists the accuracy of the instruments.

Table 3. Measuring range and accuracy of main instruments.

Instrument	Parameter	Accuracy
Analytical balance	0–2100 g	±0.1 g
Precision thermostat	−30–150 °C	±0.5 °C
Oil bath	20–300 °C	±1.0 °C
Digital absolute pressure gauge	0–110 kPa	±0.01 kPa
Precision viscometer oil bath	0–230 °C	±0.05 °C
Capillary pycnometer	50 mL	±0.03%
Ubbelohde capillary viscometer	0.36 mm, 0.46 mm, 0.58 mm, 073 mm	±0.02%
Micro reaction calorimeter	0–180 °C	±0.001 °C

3. Results and Discussion

3.1. $CaCl_2/H_2O$

To find a working pair with excellent refrigeration characteristic, the saturated vapor pressures of $CaCl_2/H_2O$ were measured and are shown in Figure 1a. Figure 1b presents the comparison of the refrigeration characteristic between $LiBr/H_2O$ and $CaCl_2/H_2O$, it shows that, for an identical pressure of 6.290 kPa, which is a typical pressure in the condenser and generator, $CaCl_2/H_2O$ had a lower generation temperature than $LiBr/H_2O$, meaning that the refrigeration characteristic of $CaCl_2/H_2O$ was better than $LiBr/H_2O$.

Figure 2 shows the absorption temperature of $CaCl_2/H_2O$ under an absorption pressure of 0.872 kPa, which corresponds to the typical evaporation temperature of 5 °C. The crystallization temperature of $CaCl_2/H_2O$ is also plotted in Figure 2 to illustrate the limitation from the crystallization of absorbent. The absorption temperature increased with increasing the concentration, and meet the crystallization temperature at 33.0 °C, which was the maximum absorption temperature under the given conditions. Generally, the absorption temperature in absorber for a refrigeration cycle is 37.0 °C, so the binary working pair of $CaCl_2/H_2O$ could not be applied for the refrigeration cycle, because of its high crystallization temperature and insufficient absorption ability.

To improve the absorption ability and reduce the crystallization temperature of $CaCl_2/H_2O$, some salts, including NaCl, KCl, LiCl, KNO_3, and $LiNO_3$, were combined with $CaCl_2/H_2O$, and their saturated vapor pressures and crystallization temperatures were measured.
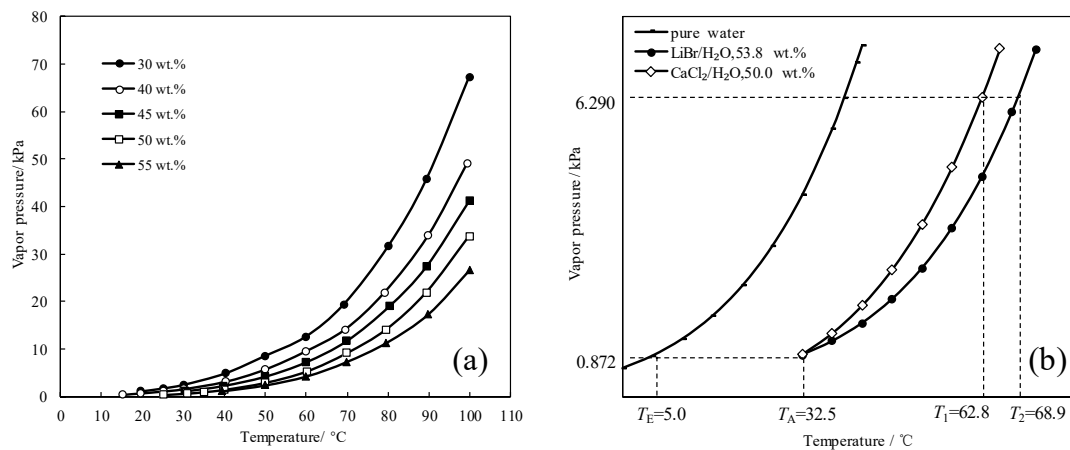
Figure 1. (**a**) Saturated vapor pressure of $CaCl_2/H_2O$; (**b**) Comparison of the refrigeration characteristic between $LiBr/H_2O$ and $CaCl_2/H_2O$.
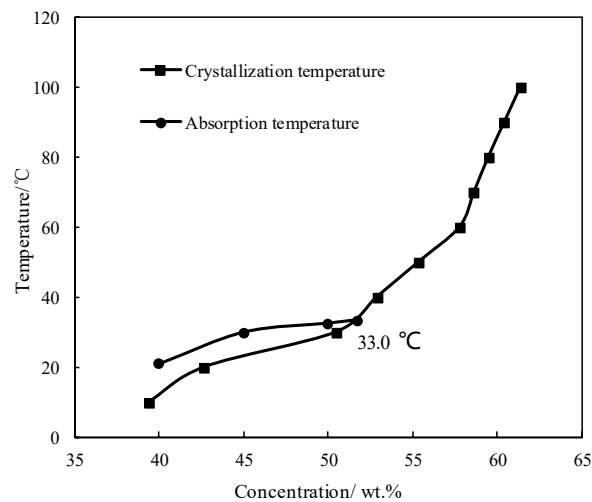
Figure 2. Crystallization temperature and absorption temperature for $CaCl_2/H_2O$.

3.2. Measurement of Crystallization Temperature T_C

The T_C of $CaCl_2$-$NaCl/H_2O$, $CaCl_2$-KCl/H_2O, $CaCl_2$-$LiCl/H_2O$, $CaCl_2$-KNO_3/H_2O, $CaCl_2$-$LiNO_3/H_2O$, and $CaCl_2$-$LiNO_3$-KNO_3/H_2O were measured. Figure 3 gives the comparison of T_C between these $CaCl_2$-based working pairs and $CaCl_2/H_2O$. Here, the concentration is the solution's total solute mass concentration.

Figure 3a shows $CaCl_2$-$NaCl/H_2O$ with adding 5.0 g NaCl to $CaCl_2/H_2O$, in which $CaCl_2$ were from 42.9 g to 61.3 g and H_2O was 95.0 g. The crystallization temperatures of $CaCl_2$-$NaCl/H_2O$ were higher than those of $CaCl_2/H_2O$ under the same concentrations.

Figure 3b shows $CaCl_2$-KCl/H_2O with adding 5.0 g KCl to $CaCl_2/H_2O$, in which $CaCl_2$ were from 78.6 g to 117.4 g and H_2O was 95.0 g. The crystallization temperatures of $CaCl_2$-KCl/H_2O were approximately 20.0 °C lower than those of $CaCl_2/H_2O$ under the same concentrations.

Figure 3c shows $CaCl_2$-$LiCl/H_2O$ with adding 10.0 g LiCl to $CaCl_2/H_2O$, in which $CaCl_2$ were from 66.7 g to 100.0 g and H_2O was 90.0 g. The crystallization temperature of $CaCl_2$-$LiCl/H_2O$ was reduced greatly when compared with that of $CaCl_2/H_2O$ at 50.0 wt.%, whereas with the concentration increasing, the effect of LiCl addition on the crystallization temperature obviously decreased.

Figure 3d shows $CaCl_2$-KNO_3/H_2O with adding 10.0 g KNO_3 to $CaCl_2/H_2O$, in which $CaCl_2$ were from 78.6 g to 117.4 g and H_2O was 90.0 g. The crystallization temperatures of $CaCl_2$-KNO_3/H_2O were lower than those of $CaCl_2/H_2O$ under the same concentrations. Moreover, it decreased with

increasing concentration in the range of 49.0 wt.% to 53.5 wt.%, whereas it increased with further increasing concentration.
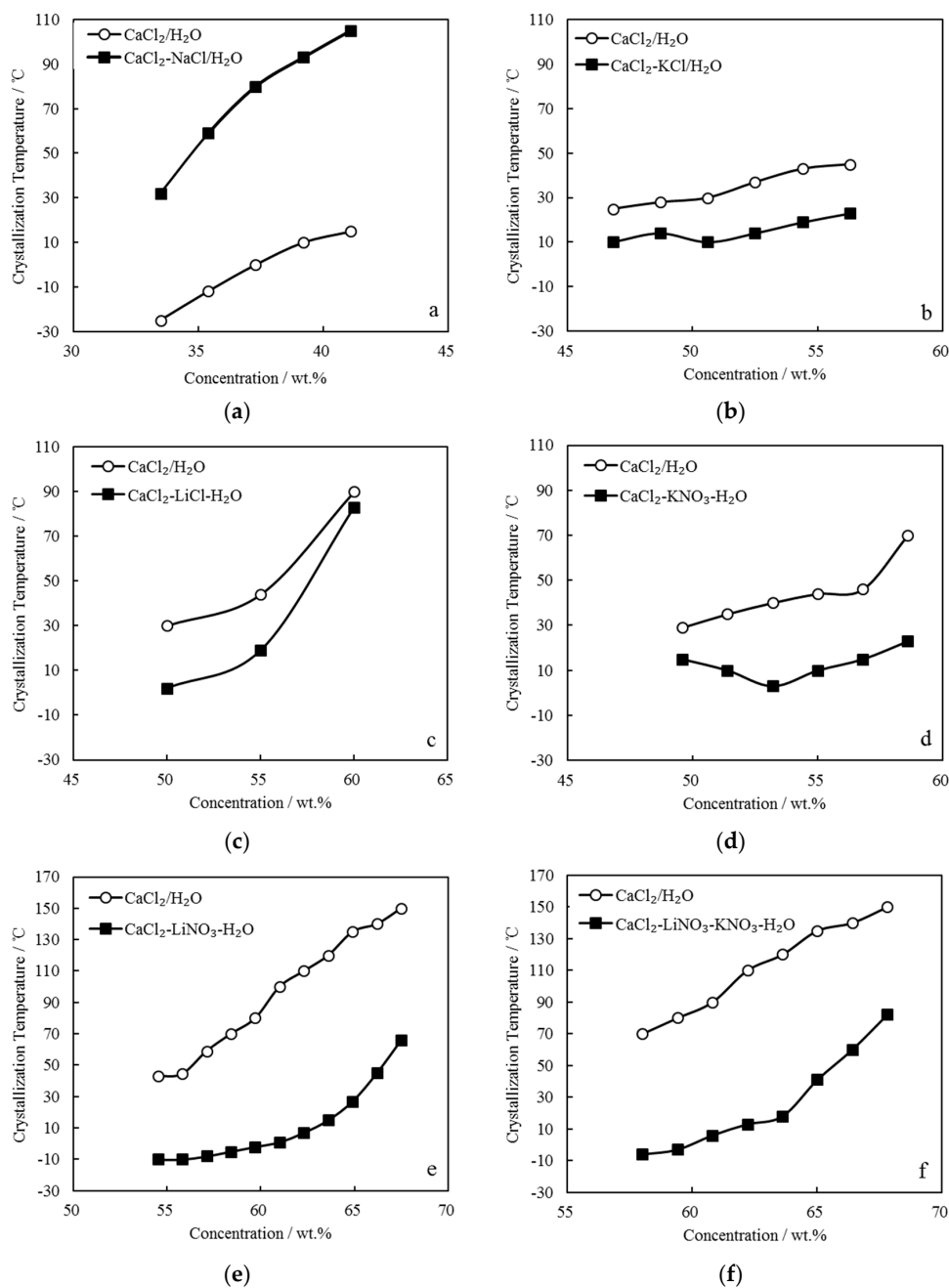
Figure 3. Comparison of T_C between $CaCl_2/H_2O$ and other $CaCl_2$-based working pairs: (**a**) $CaCl_2$-NaCl/H_2O; (**b**) $CaCl_2$-KCl/H_2O; (**c**) $CaCl_2$-LiCl/H_2O; (**d**) $CaCl_2$-KNO_3/H_2O; (**e**) $CaCl_2$-$LiNO_3$/H_2O; and, (**f**) $CaCl_2$-$LiNO_3$-KNO_3/H_2O.

Figure 3e shows $CaCl_2$-$LiNO_3$/H_2O with adding 35.0 g $LiNO_3$ to $CaCl_2/H_2O$, in which $CaCl_2$ were from 42.9 g to 100.0 g and H_2O was 65.0 g. The crystallization temperatures of $CaCl_2$-$LiNO_3$/H_2O were significantly reduced when compared with those of $CaCl_2/H_2O$ under the same concentrations. Corresponding to the concentrations ranging from 55.0 wt.% to 62.0 wt.%, which is a practical concentration range for an absorption refrigeration cycle, the crystallization temperatures of $CaCl_2$-$LiNO_3$/H_2O were from -10.0 °C to 7.0 °C, which are sufficiently low to solve the absorbent

crystallization problem in summer. However, the addition amount of 35.0 g $LiNO_3$ was relatively large, and it is a disadvantage from the aspect of cost due to $LiNO_3$ being much more expensive than $CaCl_2$.

To depress the cost increase, a part of $LiNO_3$ was replaced with KNO_3 for $CaCl_2$-$LiNO_3$/H_2O. Figure 3f shows $CaCl_2$-$LiNO_3$-KNO_3/H_2O with adding 25.0 g $LiNO_3$ and 5.0 g KNO_3 to $CaCl_2$/H_2O, in which $CaCl_2$ were from 66.7 g to 117.4 g and H_2O was 70.0 g. A reduction of crystallization temperature up to 30.0 °C was achieved from 58.0 wt.% to 65.0 wt.%, which indicated that the crystallization problem would not occur in this concentration range.

3.3. Measurement of Saturated Vapor Pressure p

p of $CaCl_2$-$LiNO_3$/H_2O and $CaCl_2$-$LiNO_3$-KNO_3/H_2O with different mass ratios were measured and are shown in Tables 4 and 5.

Table 4. p of $CaCl_2$-$LiNO_3$/H_2O with different mass ratio.

x/g		Saturated Vapor Pressure p (kPa) at Each Temperature T (°C) $CaCl_2(x)$-$LiNO_3$(35.0 g)/H_2O(65.0 g)								
42.9	T	20.0	25.0	30.5	35.0	40.0	45.3	50.4	55.7	60.2
	p	0.457	0.641	0.934	1.256	1.693	2.369	3.278	4.431	5.707
	T	65.3	70.8	75.0	80.0	85.0	90.0	95.0	100.0	
	p	7.376	9.632	11.825	15.204	19.002	23.331	28.101	34.022	
47.1	T	20.0	25.0	30.2	35.0	40.1	45.3	50.2	55.5	59.9
	p	0.419	0.585	0.834	1.138	1.535	2.139	2.948	3.998	5.136
	T	65.2	70.3	75.1	80.2	85.2	90.0	95.4	100.3	
	p	6.823	8.739	11.035	14.118	17.692	21.770	26.701	32.375	
51.5	T	20.0	25.0	29.9	35.0	40.1	45.2	50.0	55.2	59.6
	p	0.372	0.520	0.733	1.010	1.377	1.910	2.617	3.564	4.565
	T	65.1	69.8	75.2	80.4	85.3	90.0	95.8	100.6	
	p	6.269	7.846	10.244	13.031	16.382	20.208	25.300	30.728	
56.3	T	20.0	25.0	30.3	35.3	40.1	45.1	50.0	55.7	60.1
	p	0.330	0.460	0.674	0.921	1.233	1.688	2.336	3.217	4.188
	T	65.3	70.5	75.0	79.9	85.0	90.4	95.0	101.0	
	p	5.523	7.333	9.228	11.688	14.998	18.869	22.500	27.967	
61.3	T	20.1	25.0	30.3	35.2	40.2	45.1	50.1	55.3	60.0
	p	0.295	0.419	0.603	0.826	1.124	1.531	2.113	2.844	3.704
	T	65.0	70.2	75.1	80.1	85.1	90.5	95.1	100.5	
	p	4.894	6.490	8.349	10.671	13.678	17.233	20.685	25.265	
66.7	T	20.2	25.0	30.3	35.1	40.2	45.1	50.1	54.9	59.9
		0.269	0.378	0.552	0.752	1.024	1.375	1.860	2.471	3.220
	T	64.6	69.8	75.2	80.2	85.2	90.5	95.2	100.0	
		4.265	5.647	7.470	9.654	12.358	15.597	18.870	22.562	
72.4	T	20.1	25.0	30.1	35.0	40.0	44.9	50.0	55.2	60.4
	p	0.247	0.341	0.492	0.671	0.899	1.186	1.657	2.237	3.092
	T	64.6	70.0	75.0	80.4	85.1	90.0	95.5	100.2	
	p	3.930	5.268	6.678	8.678	10.960	13.507	17.127	20.709	
78.6	T	20.1	25.0	30.0	35.1	40.0	45.1	50.1	55.0	59.9
	p	0.218	0.298	0.430	0.592	0.804	1.106	1.515	2.019	2.722
	T	65.2	70.2	74.9	80.2	85.1	90.0	95.5	100.3	
	p	3.709	4.810	6.099	7.805	9.901	12.206	15.709	19.204	
85.2	T	30.1	35.0	41.1	45.0	51.1	54.9	60.0	64.9	69.9
	p	0.390	0.529	0.768	0.981	1.420	1.780	2.385	3.205	4.185
	T	75.0	80.2	85.3	90.2	95.4	100.6			
	p	5.624	7.135	9.098	10.996	13.756	17.535			
92.3	T	45.1	50.1	54.9	60.8	65.4	70.2	75.5	81.1	85.1
	p	0.886	1.188	1.645	2.303	3.048	3.903	5.226	6.777	8.311
	T	90.5	95.8	100.0						
	p	10.276	12.820	15.447						
100.0	T	65.7	70.4	76.7	80.2	85.1	90.2	95.2	100.1	
	p	2.711	3.552	5.050	6.000	7.432	9.260	11.383	13.858	

Table 5. p of $CaCl_2$-$LiNO_3$-KNO_3/H_2O with different mass ratio.

y/g		Saturated Vapor Pressure p (kPa) at Each Temperature T (°C) $CaCl_2(y)$-$LiNO_3$(25.0 g)-KNO_3(5.0 g)/H_2O(70.0 g)								
66.7	T	20.0	25.0	30.1	35.5	40.0	45.3	50.0	54.9	60.0
	p	0.352	0.511	0.741	1.064	1.434	1.987	2.638	3.508	4.660
	T	65.1	70.1	75.2	80.0	87.2	89.9	95.0	100.0	
	p	6.119	8.024	10.490	13.001	17.346	19.223	23.450	28.590	
72.4	T	20.0	25.0	30.2	34.9	40.6	45.6	50.0	55.2	60.4
	p	0.315	0.455	0.650	0.911	1.353	1.850	2.403	3.250	4.283
	T	65.1	69.9	75.2	80.3	85.0	89.7	94.9	100.0	
	p	5.560	7.106	9.469	11.911	14.327	17.200	21.021	26.025	
78.6	T	20.0	25.0	29.9	35.1	40.0	45.0	50.0	54.9	60.0
	p	0.259	0.371	0.530	0.762	1.049	1.427	1.940	2.634	3.552
	T	65.1	69.8	75.5	80.1	85.0	89.9	94.9	100.1	
	p	4.825	6.306	8.546	10.555	12.913	15.540	18.898	23.535	
85.2	T	20.0	25.0	30.0	35.0	40.5	45.0	50.0	55.0	60.2
	p	0.219	0.312	0.445	0.627	0.928	1.239	1.740	2.311	3.200
	T	65.0	69.8	75.1	80.0	85.1	90.0	95.2	100.2	
	p	4.205	5.499	7.402	9.378	11.789	17.909	21.505		
92.3	T	20.0	25.0	30.0	35.4	39.9	45.0	50.0	55.1	60.1
	p	0.198	0.285	0.399	0.581	0.793	1.136	1.563	2.150	2.925
	T	65.2	70.0	75.3	79.9	85.2	90.0	95.5	100.2	
	p	3.875	5.048	6.683	8.448	10.859	13.429	16.906	19.867	
100.0	T	41.0	44.9	50.0	55.0	60.2	65.0	70.1	75.1	80.3
	p	0.673	0.889	1.244	1.730	2.454	3.349	4.519	5.911	7.656
	T	85.2	89.9	94.9	99.9					
	p	9.761	12.060	14.960	18.163					
108.3	T	60.0	65.2	70.0	75.2	80.1	84.8	90.4	95.1	100.1
	p	2.205	3.045	4.051	5.252	6.686	8.464	10.993	13.110	15.587
117.4	T	82.0	85.1	90.0	95.0	100.3				
	p	5.921	6.971	9.009	11.303	14.387				

The measured p was fitted by Equation (1) [33–35].

$$\log p = \sum_{i=0}^{4} [A_i + B_i/(T + 273.15 - C_i)]w^i \tag{1}$$

where A_i, B_i, and C_i are the regression parameters. Equation (2) obtains the average absolute relative deviation (AARD) between the measured values and the fitted values.

$$\text{AARD} = 1/N \sum_{i=1}^{N} \left| (P_{\exp} - P_{fit})/P_{fit} \right| \tag{2}$$

where N is total number of data, $P_{\exp}$ is the measured or obtained value, and P_{fit} is the fitted value.

The regression parameters and AARD were obtained and are shown in Tables 6 and 7, respectively.

Figures 4 and 5 plot the measured p and fitted value of $CaCl_2$-$LiNO_3$/H_2O and $CaCl_2$-$LiNO_3$-KNO_3/H_2O, respectively. The fitted value agreed well with the measured p. 60.2 wt.% for $CaCl_2$(63.2 g)-$LiNO_3$(35.0 g)/H_2O(65.0 g) and 60.5 wt.% for $CaCl_2$(77.3 g)-$LiNO_3$(25.0 g)-KNO_3(5.0 g)/H_2O(70.0 g) were obtained, respectively, by Equation (1) at 37.0 °C and 0.872 kPa, which are the typical absorption temperature and absorption pressure for a refrigeration cycle. Meanwhile, the absorption temperatures of these two working pairs were 70.5 °C and 69.2 °C, respectively, at 6.290 kPa, which is the typical generation pressure. Therefore, $CaCl_2$(77.3 g)-$LiNO_3$(25.0 g)-KNO_3(5.0 g)/H_2O(70.0 g),

with a solute mass ratio of 15.5:5:1, had been proposed as an alternative working pair for LiBr/H_2O. The proposed working pair is expressed as $CaCl_2$-$LiNO_3$-KNO_3(15.5:5:1)/H_2O in this paper.

Table 6. Regression parameters for $CaCl_2$-$LiNO_3$/H_2O and average absolute relative deviation (AARD) value.

i	A_i	B_i	C_i	AARD
0	4.896×10^{-1}	-1.985×10^{0}	-3.624×10^{0}	
1	-1.172×10^{-1}	5.756×10^{-1}	-1.189×10^{1}	
2	1.024×10^{-2}	-2.990×10^{-1}	-3.963×10^{1}	1.55%
3	-1.768×10^{-4}	3.046×10^{-3}	-1.894×10^{1}	
4	9.452×10^{-7}	-8.957×10^{-6}	-4.335×10^{0}	

Table 7. Regression parameters for $CaCl_2$-$LiNO_3$-KNO_3/H_2O and AARD value.

i	A_i	B_i	C_i	AARD
0	-2.262×10^{-2}	-3.844×10^{-1}	5.668×10^{-1}	
1	5.616×10^{-1}	1.184×10^{0}	1.367×10^{0}	
2	-2.523×10^{-2}	-1.498×10^{-2}	5.033×10^{0}	2.34%
3	4.274×10^{-4}	-3.524×10^{-3}	-3.042×10^{1}	
4	-2.421×10^{-6}	2.944×10^{-5}	-1.620×10^{1}	
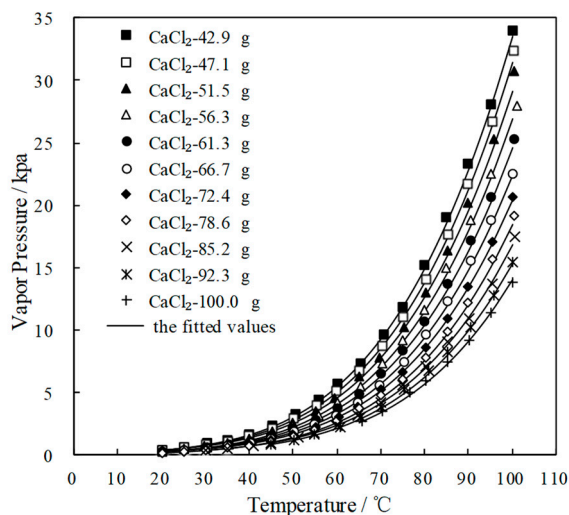
Figure 4. *p* of $CaCl_2$-$LiNO_3$/H_2O with different mass ratio.
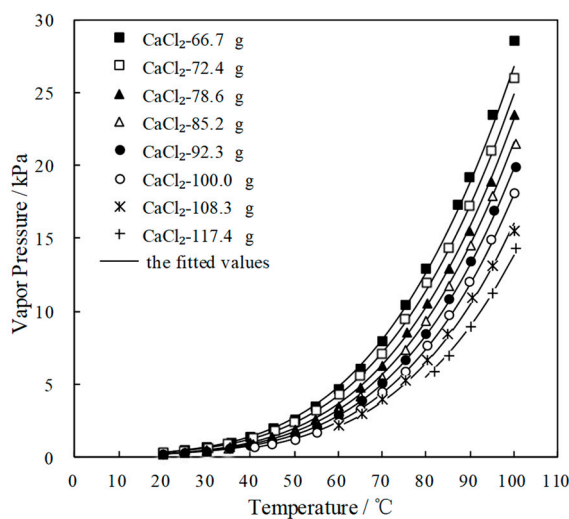
Figure 5. *p* of $CaCl_2$-$LiNO_3$-KNO_3/H_2O with different mass ratio.

The *p* of this working pair was measured in order to analyze the cycle performance with CaCl$_2$-LiNO$_3$-KNO$_3$(15.5:5:1)/H$_2$O, as shown in Table 8.

Table 8. *p* of CaCl$_2$-LiNO$_3$-KNO$_3$(15.5:5:1)/H$_2$O.

w/wt.%		Saturated Vapor Pressure *p* (kPa) at Each Temperature *T* (°C)								
50.0	*T*	20.1	25.7	30.2	35.3	40.6	45.0	50.7	55.4	60.0
	p	0.634	0.901	1.225	1.705	2.371	3.064	4.325	5.626	7.206
	T	65.2	70.7	75.0	80.9	85.7	90.0	95.2	100.0	
	p	9.336	12.075	14.800	19.100	23.536	27.931	33.519	40.578	
55.0	*T*	21.2	28.0	32.1	35.0	39.9	45.1	52.0	55.6	60.0
	p	0.443	0.712	0.939	1.148	1.569	2.210	3.407	4.249	5.387
	T	65.2	70.2	75.0	80.9	85.0	90.4	95.0	100.0	
	p	7.060	9.016	11.301	14.825	17.699	21.912	26.011	31.898	
60.0	*T*	21.0	26.1	30.0	35.0	41.0	45.0	50.0	55.1	60.4
	p	0.280	0.412	0.541	0.769	1.166	1.492	2.071	2.855	4.026
	T	65.5	70.2	75.0	80.0	85.4	90.4	95.2	100.1	
	p	5.355	6.901	8.873	11.106	14.063	17.268	21.176	25.912	
65.0	*T*	25.1	30.0	35.0	40.5	45.0	50.0	55.6	60.5	65.6
	p	0.226	0.341	0.490	0.744	0.985	1.339	1.958	2.675	3.665
	T	71.1	75.4	80.1	85.2	90.0	94.6	100.5		
	p	4.971	6.282	7.749	9.894	12.395	15.241	19.243		

The measured *p* was fitted by Equation (3) and the AARD was obtained to be 1.82% by Equation (2).

$$
\begin{aligned}
\log p = {} & 1.243 - 8.293/(T + 273.15 + 3.466 \times 10^3) + \\
& (1.698 \times 10^{-1} - 3.894 \times 10/(T + 273.15 + 1.944 \times 10^2)) \times w + \\
& (-1.503 \times 10^{-3} + 3.797 \times 10^{-1}/(T + 273.15 + 2.836 \times 10^2)) \times w^2
\end{aligned} \tag{3}
$$

Figure 6 shows the measured *p* and fitted value. The measured *p* agreed well with the fitted value, which indicated that the *p* of CaCl$_2$-LiNO$_3$-KNO$_3$(15.5:5:1)/H$_2$O could be obtained with the given corresponding concentration and temperature.
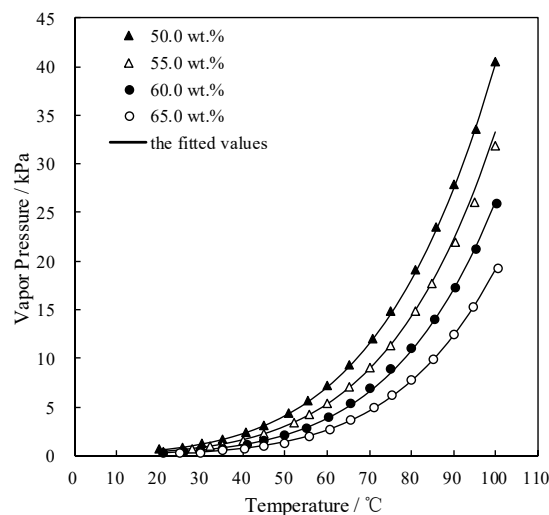
Figure 6. *p* of CaCl$_2$-LiNO$_3$-KNO$_3$(15.5:5:1)/H$_2$O.

Figure 7 compares the refrigeration characteristic of CaCl$_2$-LiNO$_3$-KNO$_3$(15.5:5:1)/H$_2$O and LiBr/H$_2$O. The generation temperature of CaCl$_2$-LiNO$_3$-KNO$_3$(15.5:5:1)/H$_2$O was 74.0 °C, which was 7.0 °C lower than that of LiBr/H$_2$O. In other words, the temperature that is required for the driving heat source could be reduced by 7.0 °C through using CaCl$_2$-LiNO$_3$-KNO$_3$(15.5:5:1)/H$_2$O instead of LiBr/H$_2$O.
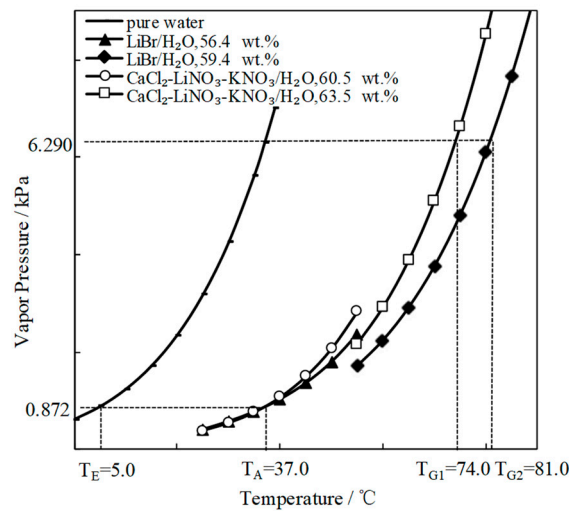
Figure 7. Comparison of the refrigeration characteristic between LiBr/H_2O and $CaCl_2$-$LiNO_3$-KNO_3 (15.5:5:1)/H_2O.

3.4. Measurement of Density ρ

ρ of $CaCl_2$-$LiNO_3$-KNO_3(15.5:5:1) /H_2O was measured by a capillary pycnometer method. Table 9 lists the results.

Table 9. ρ of $CaCl_2$-$LiNO_3$-KNO_3(15.5:5:1)/H_2O.

w/wt.%		Density ρ (g·cm^{-3}) at Each Temperature T (°C)								
50.0	T	20.0	30.0	40.0	50.0	60.0	70.0	80.0	90.0	100.0
	ρ	1.4614	1.4563	1.4488	1.4412	1.4352	1.4278	1.4215	1.4141	1.4067
55.0	T	20.0	30.0	40.0	50.0	60.0	70.0	80.0	90.0	100.0
	ρ	1.5181	1.5111	1.5042	1.4977	1.4906	1.4834	1.4761	1.4696	1.4618
60.0	T	20.0	30.0	40.0	50.0	60.0	70.0	80.0	90.0	100.0
	ρ	1.5784	1.5713	1.5642	1.5547	1.5495	1.5420	1.5351	1.5287	1.5229
65.0	T			40.0	50.0	60.0	70.0	80.0	90.0	100.0
	ρ			1.6245	1.6185	1.6131	1.6058	1.5991	1.5915	1.5820

The measured ρ of $CaCl_2$-$LiNO_3$-KNO_3(15.5:5:1)/H_2O was fitted by Equation (4) and AARD was obtained to be 0.22% by Equation (2).

$$
\begin{aligned}
\rho = {} & 1.923 \times 10^2 - 1.139 \times (T + 273.15) + 1.690 \times 10^{-3} \times (T + 273.15)^2 \\
& + (-1.034 \times 10^3 + 6.162 \times (T + 273.15) - 9.146 \times 10^{-3} \times (T + 273.15)^2) \times w \\
& + (1.859 \times 10^3 - 1.107 \times 10 \times (T + 273.15) + 1.642 \times 10^{-2} \times (T + 273.15)^2) \times w^2 \\
& + (-1.108 \times 10^3 + 6.595 \times (T + 273.15) - 9.781 \times 10^{-3} \times (T + 273.15)^2) \times w^3
\end{aligned}
\tag{4}
$$

Figure 8 shows the measured ρ and the fitted value. The measured ρ was highly consistent with the fitted value. The density linearly decreased with the temperature increasing, and it increased with the concentration increasing.
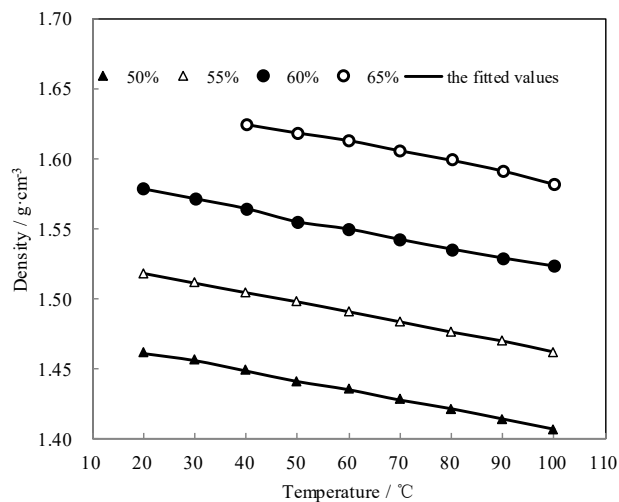
Figure 8. ρ of CaCl$_2$-LiNO$_3$-KNO$_3$(15.5:5:1)/H$_2$O.

3.5. Measurement of Viscosity η

η of CaCl$_2$-LiNO$_3$-KNO$_3$(15.5:5:1)/H$_2$O was measured by the Ubbelohde capillary viscometer method. Table 10 shows the results.

Table 10. η of CaCl$_2$-LiNO$_3$-KNO$_3$(15.5:5:1)/H$_2$O.

w/wt.%		Viscosity η (mPa·s) at Each Temperature T (°C)								
50.0	T	20.0	30.0	40.0	50.0	60.0	70.0	80.0	90.0	100.0
	H	20.13	14.51	10.56	8.00	5.98	4.77	4..11	3.47	2.95
55.0	T	20.0	30.0	40.0	50.0	60.0	70.0	80.0	90.0	100.0
	H	45.51	29.57	21.63	15.40	11.42	7.79	6.19	5.18	4.35
60.0	T	20.0	30.0	40.0	50.0	60.0	70.0	80.0	90.0	100.0
	H	144.05	81.88	51.66	33.48	24.07	16.91	12.51	9.47	7.71
65.0	T			40.0	50.0	60.0	70.0	80.0	90.0	100.0
	H			144.90	80.97	52.26	37.07	25.91	19.38	14.55

The measured η of CaCl$_2$-LiNO$_3$-KNO$_3$(15.5:5:1)/H$_2$O was fitted by Equation (5) and the AARD was obtained to be 0.82% by Equation (2).

$$
\begin{aligned}
\eta = {} & 8.099 \times 10 - 4.721 \times 10^4/(T+273.15) + 8.480 \times 10^6/(T+273.15)^2 \\
& + (-2.286 \times 10^2 + 1.169 \times 10^5/(T+273.15) - 2.278 \times 10^7/(T+273.15)^2) \times w \\
& + (2.534 \times 10 - 1.816 \times 10^4/(T+273.15) - 4.422 \times 10^5/(T+273.15)^2) \times w^2 \\
& + (2.224 \times 10^2 + 4.127 \times 10^5/(T+273.15) + 2.716 \times 10^7/(T+273.15)^2) \times w^3
\end{aligned}
\tag{5}
$$

Figure 9 shows the measured η and the fitted value. The measured η agreed well with the fitted value. η exponentially decreased with the temperature increasing, whereas it increased with the concentration increasing.
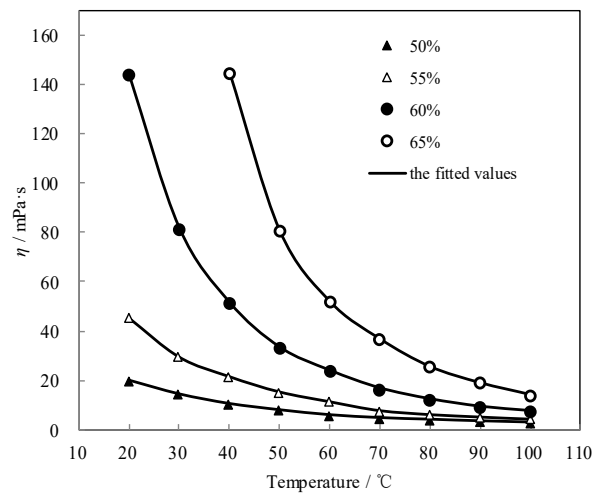
Figure 9. η of $CaCl_2$-$LiNO_3$-KNO_3(15.5:5:1)/H_2O.

3.6. Measurement of Specific Heat Capacity C_p

C_p of $CaCl_2$-$LiNO_3$-KNO_3(15.5:5:1)/H_2O was measured with a micro reaction calorimeter. Table 11 lists the results.

Table 11. C_p of $CaCl_2$-$LiNO_3$-KNO_3(15.5:5:1)/H_2O.

w/wt.%		Specific Heat Capacity C_p (kJ·kg^{-1}·K^{-1}) at Each Temperature T (°C)									
50.0	T	10.0	20.0	30.0	40.0	50.0	60.0	70.0	80.0	90.0	100.0
	C_p	2.438	2.444	2.458	2.473	2.487	2.501	2.518	2.527	2.542	2.563
55.0	T	10.0	20.0	30.0	40.0	50.0	60.0	70.0	80.0	90.0	100.0
	C_p	2.313	2.321	2.335	2.350	2.366	2.380	2.400	2.417	2.432	2.452
60.0	T	10.0	20.0	30.0	40.0	50.0	60.0	70.0	80.0	90.0	100.0
	C_p	2.189	2.193	2.206	2.216	2.227	2.241	2.254	2.266	2.286	2.303
65.0	T	10.0	20.0	30.0	40.0	50.0	60.0	70.0	80.0	90.0	100.0
	C_p	2.039	2.045	2.057	2.071	2.085	2.098	2.110	2.127	2.130	2.146

The measured C_p was fitted by Equation (6) and AARD was obtained to be 0.21% by Equation (2).

$$
\begin{aligned}
C_p = {} & 2.575 + 1.951 \times 10^{-2} \times (T + 273.15) - 2.200 \times 10^{-4} \times (T + 273.15)^2 \\
& + \left(1.121 \times 10^{-2} - 6.433 \times 10^{-4} \times (T + 273.15) + 7.593 \times 10^{-6} \times (T + 273.15)^2\right)w \\
& + \left(-3.259 \times 10^{-4} + 5.570 \times 10^{-6} \times (T + 273.15) - 7.020 \times 10^{-8} \times (T + 273.15)^2\right)w^2
\end{aligned}
\tag{6}
$$

Figure 10 shows the measured C_p and the fitted value. C_p linearly increased with increasing the temperature.
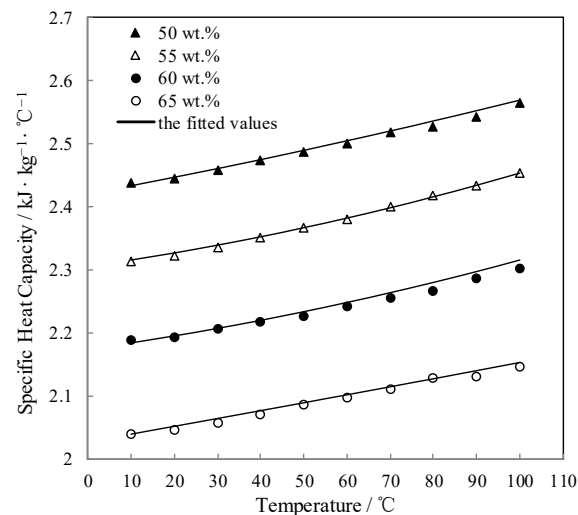
Figure 10. C_p of CaCl$_2$-LiNO$_3$-KNO$_3$(15.5:5:1) /H$_2$O.

3.7. Calculation of Specific Enthalpy h

3.7.1. C$_p$ of CaCl$_2$, LiNO$_3$, KNO$_3$ and H$_2$O

The C_p of solid KNO$_3$ was measured and is shown in Table 12, C_p of CaCl$_2$, LiNO$_3$, and H$_2$O are given in Reference Literature [29].

Table 12. C_p of solid KNO$_3$ at atmosphere pressure.

Reagent		Specific Heat Capacity C_p (kJ·kg^{-1}·K^{-1}) at Each Temperature T (°C)									
KNO$_3$	T	10.0	20.0	30.0	40.0	50.0	60.0	70.0	80.0	90.0	100.0
	C_p	0.930	0.952	0.968	0.974	0.988	1.040	1.053	1.072	1.090	1.119

3.7.2. Measurement of Dissolution Enthalpy ΔH$_{mix}$

ΔH_{mix} of KNO$_3$, LiNO$_3$, and CaCl$_2$ with a mass ratio of 15.5:5:1 were measured at 25.0 °C and are shown in Table 13.

Table 13. ΔH_{mix} of CaCl$_2$-LiNO$_3$-KNO$_3$(15.5:5:1) /H$_2$O at 25.0 °C.

w/wt.%	50.0	55.0	60.0	65.0
ΔH_{mix}/kJ·kg^{-1}	149.310	150.501	150.275	151.292

3.7.3. Calculation of Specific Enthalpy h

h of CaCl$_2$-LiNO$_3$-KNO$_3$(15.5:5:1)/H$_2$O can be obtained from the measured C_p and ΔH_{mix} [25,36,37]. Table 14 lists the obtained results.

The obtained h was fitted by Equation (7) and AARD was obtained to be 0.07% by Equation (2).

$$
\begin{aligned}
h = &\ 3.151 \times 10^2 - 1.193 \times w + 6.998 \times 10^{-3} \times w^2 \\
&+ (2.971 - 2.553 \times 10^{-3} \times w - 1.817 \times 10^{-4} \times w^2)(T + 273.15) \\
&+ (-1.775 \times 10^{-3} + 1.198 \times 10^{-4} \times w - 1.304 \times 10^{-6} \times w^2)(T + 273.15)^2
\end{aligned}
\tag{7}
$$

Figure 11 shows the obtained h and the fitted value. h linearly increased with increasing the temperature, and the slope of line slightly increased with reducing the concentration.

Table 14. *h* of CaCl$_2$-LiNO$_3$-KNO$_3$(15.5:5:1)/H$_2$O.

w/wt.%		Specific Enthalpy *h* (kJ·kg^{-1}) at Each Temperature *T* (°C)									
50.0	*T*	10.0	20.0	30.0	40.0	50.0	60.0	70.0	80.0	90.0	100.0
	h	296.787	321.185	345.720	370.395	395.214	420.183	445.305	470.584	496.025	521.632
55.0	*T*	10.0	20.0	30.0	40.0	50.0	60.0	70.0	80.0	90.0	100.0
	h	293.028	316.239	339.568	363.026	386.622	410.368	434.272	458.345	482.598	507.039
60.0	*T*	10.0	20.0	30.0	40.0	50.0	60.0	70.0	80.0	90.0	100.0
	h	290.874	312.767	334.776	356.907	379.172	401.578	424.134	446.849	469.733	492.793
65.0	*T*	10.0	20.0	30.0	40.0	50.0	60.0	70.0	80.0	90.0	100.0
	h	287.666	308.113	328.685	349.382	370.205	391.155	412.233	433.438	454.773	476.237
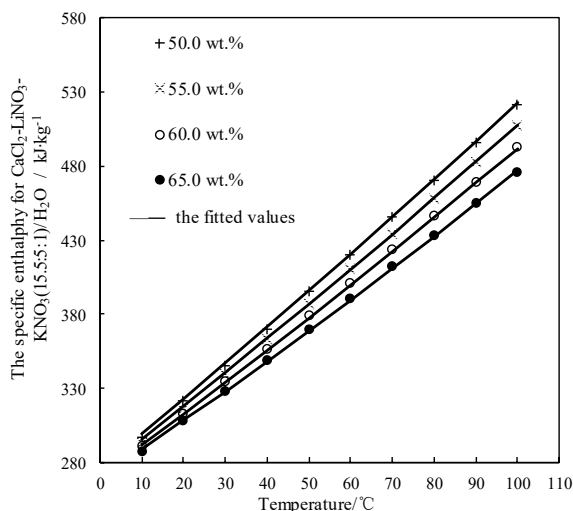
Figure 11. *h* of CaCl$_2$-LiNO$_3$-KNO$_3$(15.5:5:1) /H$_2$O.

3.8. Calculation of Specific Entropy s

s of a solution can be also obtained from the measured C_p and ΔH_{mix} [38]. *s* of CaCl$_2$-LiNO$_3$-KNO$_3$(15.5:5:1) /H$_2$O was obtained and is shown in Table 15.

Table 15. *s* of CaCl$_2$-LiNO$_3$-KNO$_3$(15.5:5:1)/H$_2$O.

w/wt.%		Entropy *s* (kJ·kg^{-1}·K^{-1}) at Each Temperature *T* (°C)									
50.0	*T*	10.0	20.0	30.0	40.0	50.0	60.0	70.0	80.0	90.0	100.0
	s	1.412	1.496	1.578	1.658	1.736	1.813	1.889	1.963	2.036	2.108
55.0	*T*	10.0	20.0	30.0	40.0	50.0	60.0	70.0	80.0	90.0	100.0
	s	1.417	1.498	1.576	1.652	1.727	1.800	1.872	1.943	2.014	2.083
60.0	*T*	10.0	20.0	30.0	40.0	50.0	60.0	70.0	80.0	90.0	100.0
	s	1.422	1.500	1.574	1.645	1.716	1.785	1.852	1.919	1.985	2.050
65.0	*T*	10.0	20.0	30.0	40.0	50.0	60.0	70.0	80.0	90.0	100.0
	s	1.431	1.502	1.571	1.638	1.704	1.769	1.832	1.895	1.955	2.016

The obtained *s* of CaCl$_2$-LiNO$_3$-KNO$_3$(15.5:5:1) /H$_2$O was fitted by Equation (8) and the AARD was obtained to be 0.84% by Equation (2).

$$
\begin{aligned}
s = {} & -2.662 \times 10 + 1.370 \times 10^2 \times w - 2.828 \times 10^2 \times w^2 + 1.967 \times 10^2 \times w^3 \\
& + (2.333 \times 10^{-1} + 1.315 \times w + 2.735 \times w^2 - 1.892 \times w^3)(T + 273.15) + \\
& (-6.999 \times 10^{-4} + 4.199 \times 10^{-3} \times w - 8.788 \times 10^{-3} \times w^2 + 6.062 \times 10^{-3} \times w^3)(T + 273.15)^2 \\
& + (7.282 \times 10^{-7} - 4.461 \times 10^{-6} \times w + 9.373 \times 10^{-6} \times w^2 - 6.469 \times 10^{-6} \times w^3)(T + 273.15)^3
\end{aligned}
\tag{8}
$$

Figure 12 shows the obtained *s* and the fitted value. *s* increased with the temperature increasing and decreased with the concentration increasing when the temperature was above 28 °C, whereas it changed little with the concentration when the temperature was below 28 °C.
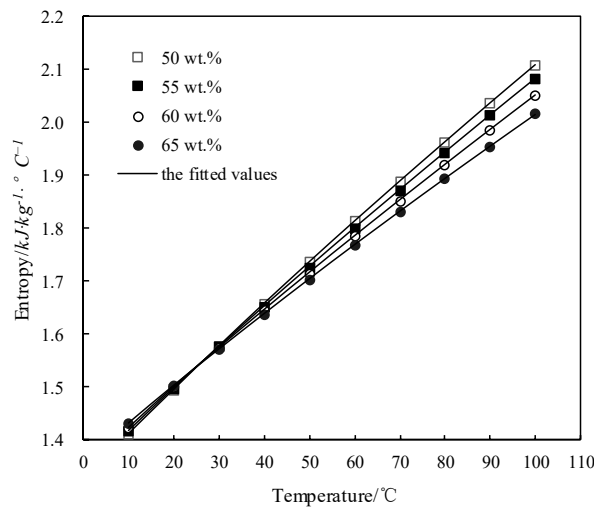
Figure 12. *s* of $CaCl_2$-$LiNO_3$-KNO_3(15.5:5:1)/H_2O.

3.9. Application for an Absorption Refrigeration Cycle

3.9.1. Absorption Refrigeration Cycle Using $CaCl_2$-$LiNO_3$-KNO_3(15.5:5:1)/H_2O

Figure 13a shows the schematic of an absorption refrigeration cycle. Figure 13b is the *P-T* diagram of the cycle, and the points that are marked in the two diagrams are one-to-one correspondence.
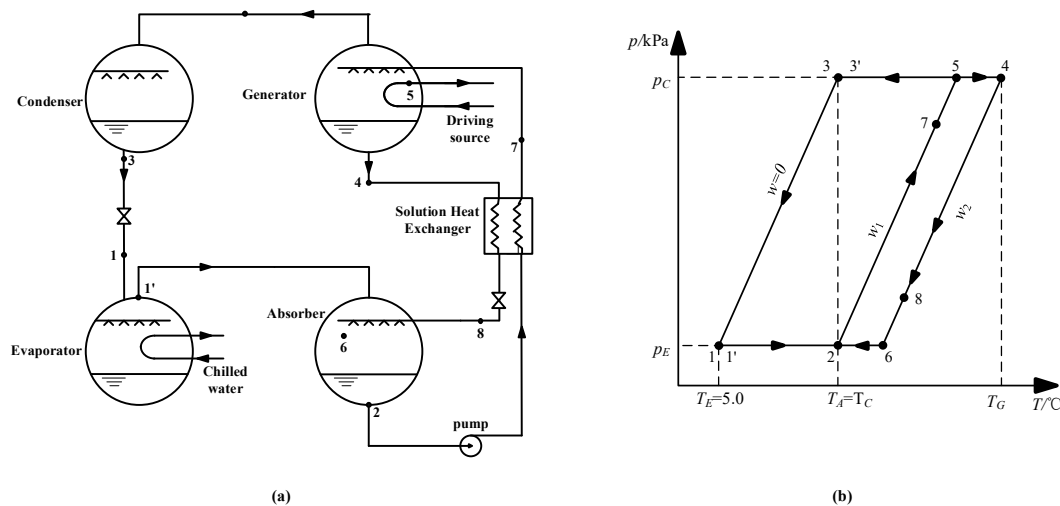
Figure 13. (**a**) Schematic of the absorption refrigeration cycle; (**b**) *P-T* diagram of the absorption refrigeration cycle.

The working conditions are given, as follows: the evaporation temperature was 5.0 °C; the absorption temperature and condensation temperature were 37.0 °C; and, the evaporation and condensation pressures were 0.872 kPa and 6.290 kPa, respectively. The concentration of dilute solution for $CaCl_2$-$LiNO_3$-KNO_3(15.5:5:1)/H_2O was figured out to be 60.5 wt.% by Equation (3), and the strong solution was 63.5 wt.%, with a concentration difference of 3.0 wt.%, thus, the generation temperature of the cycle was determined to be 74.0 °C by Equation (3). The same method was applied to calculate the generation temperature while using $LiBr/H_2O$ and other $CaCl_2$-based

working pairs, including $CaCl_2$-LiBr-$LiNO_3$-KNO_3(16.2:2:2:1)/H_2O, $CaCl_2$-$LiNO_3$-LiBr(8.72:1:1)/H_2O, and $CaCl_2$-LiBr(1.35:1)/H_2O. Table 16 lists the results.

Table 16. Concentration and generation temperature for different working pairs.

Working Pair	$CaCl_2$-$LiNO_3$-KNO_3 (15.5:5:1)/H_2O	LiBr/ H_2O	$CaCl_2$-LiBr-$LiNO_3$-KNO_3(16.2:2:2:1) /H_2O	$CaCl_2$-$LiNO_3$-LiBr (8.72:1:1)/H_2O	$CaCl_2$-LiBr (1.35:1) /H_2O
Dilute solution/wt.%	60.5	56.4	58.5	57.3	55.8
Strong solution/wt.%	63.5	59.4	61.5	60.3	58.8
Generation temperature/°C	74.0	81.0	74.8	73.3	74.8

As seen in Table 16, the generation temperature was reduced by 7.0 °C through the use of $CaCl_2$-$LiNO_3$-KNO_3(15.5:5:1)/H_2O instead of LiBr/H_2O. The generation temperature differences between the four $CaCl_2$-based working pairs were relatively small.

3.9.2. Analysis of COP and Exergy Efficiency

To analyze the performance of a refrigeration cycle with $CaCl_2$-$LiNO_3$-KNO_3(15.5:5:1)/H_2O, the state parameters of typical points in Figure 13 were obtained by Equations (3), (7) and (8). Table 17 lists the results.

Table 17. State parameters of streams in the cycle with $CaCl_2$-$LiNO_3$-KNO_3(15.5:5:1)/H_2O.

Point	Stream	p/kPa	T/°C	w/wt.%	h/kJ·kg^{-1}	D/kg·s^{-1}	s/kJ·kg^{-1}·K^{-1}
1	Water	0.872	5.0	0	439.6	1.0	0.07621
1′	Vapor	0.872	5.0	0	2927.9	1.0	9.02690
2	Dilute solution	0.872	37.0	60.5	349.2	21.2	0.09149
3	Water	6.290	37.0	0	573.5	1.0	0.53190
4	Strong solution	6.290	74.0	63.5	424.4	20.2	0.33201
4′	Vapor	6.290	74.0	0	3054.2	1.0	8.5368
5	Dilute solution	6.290	69.2	60.5	420.9	21.2	0.31351
6	Strong solution	0.872	41.0	63.5	353.7	20.2	0.11525
7	Dilute solution	–	63.9	60.5	409.9	21.2	0.27782
8	Strong solution	–	44.3	63.5	360.7	20.2	0.13754

The coefficient of performance (COP) for the absorption refrigeration cycle can be defined as:

$$\text{COP} = \frac{Q_E}{Q_G} = \frac{h_{1'} - h_3}{h_{4'} - h_4 + \alpha(h_4 - h_7)} \tag{9}$$

where α represents circulating ratio.

COP was obtained to be 0.801 when using $CaCl_2$-$LiNO_3$-KNO_3(15.5:5:1)/H_2O as the working pair. The COPs for other working pairs were obtained with the same method, and the results are listed in Table 18.

Table 18. Coefficient of performance (COP) of the cycle with different working pairs.

Working Pair	CaCl$_2$-LiNO$_3$-KNO$_3$ (15.5:5:1) /H$_2$O	LiBr /H$_2$O	CaCl$_2$-LiBr-LiNO$_3$-KNO$_3$ (16.2:2:2:1) /H$_2$O	CaCl$_2$-LiNO$_3$-LiBr (8.72:1:1) /H$_2$O	CaCl$_2$-LiBr (1.35:1) /H$_2$O
COP	0.801	0.762	0.793	0.805	0.788

Table 18 shows that, through using CaCl$_2$-LiNO$_3$-KNO$_3$(15.5:5:1)/H$_2$O instead of LiBr/H$_2$O, the COP was improved by 0.04. Moreover, the exergy destruction in each part of the cycle were analyzed to further compare the performance between CaCl$_2$-LiNO$_3$-KNO$_3$(15.5:5:1)/H$_2$O and LiBr/H$_2$O. Exergy is defined as the maximum possible reversible work that can be obtained from a stream:

$$E = (h - h_0) - (T_0 + 273.15)(s - s_0) \tag{10}$$

where T_0 represents the environment temperature that was taken as 25 °C in this paper.

The exergy destructions for each part of the absorption refrigeration cycle were obtained as follows [39].

Evaporator:

$$\Delta E_E = D_3 E_3 - D_{1'} E_{1'} + Q_E \left(\frac{T_0}{T_E} - 1 \right) \tag{11}$$

Condenser:

$$\Delta E_C = D_{4'} E_{4'} - D_3 E_3 - Q_C \left(1 - \frac{T_0}{T_C} \right) \tag{12}$$

Absorber:

$$\Delta E_A = D_8 E_8 + D_{1'} E_{1'} - D_2 E_2 - Q_A \left(1 - \frac{T_0}{T_A} \right) \tag{13}$$

Generator:

$$\Delta E_G = D_7 E_7 - D_4 E_4 - D_{4'} E_{4'} + Q_G \left(1 - \frac{T_0}{T_G} \right) \tag{14}$$

Heat exchanger:

$$\Delta E_{HEX} = D_2 E_2 + D_4 E_4 - D_7 E_7 - D_8 E_8 \tag{15}$$

Table 19 compares the exergy destructions of the absorption cycle with CaCl$_2$-LiNO$_3$-KNO$_3$(15.5:5:1)/H$_2$O and LiBr/H$_2$O. Except the exergy destruction of the evaporator was equal because of the same evaporation condition, the exergy destructions of other parts for CaCl$_2$-LiNO$_3$-KNO$_3$(15.5:5:1)/H$_2$O were lower than those for LiBr/H$_2$O. For the absorption refrigeration cycle, the exergy efficiency (η_E) can be defined as:

$$\eta_E = \frac{Q_E (T_E / T_0 - 1)}{Q_G (1 - T_Q / T_0)} \tag{16}$$

Table 19. The exergy destruction in each part of absorption refrigeration cycle using CaCl$_2$-LiNO$_3$-KNO$_3$(15.5:5:1)/H$_2$O and LiBr/H$_2$O.

Part	Exergy Destruction/kW	
	CaCl$_2$-LiNO$_3$-KNO$_3$ (15.5:5:1)/H$_2$O	LiBr/H$_2$O
Evaporator	0.5	0.5
Condenser	0.4	0.8
Absorber	52.1	55.3
Generator	282.6	332.7
Heat exchanger	25.5	31.4

The η_E of the absorption refrigeration cycle with $CaCl_2$-$LiNO_3$-KNO_3(15.5:5:1)/H_2O and $LiBr$/H_2O were obtained to be 0.327 and 0.272, respectively. When compared with COP, the difference in exergy efficiency between the two working pairs was more distinct, which further showed the advantage of $CaCl_2$-$LiNO_3$-KNO_3(15.5:5:1)/H_2O as an alternative working pair.

Figures 14 and 15 show the changes of generation temperature and efficiencies (COP and η_E) for $CaCl_2$-$LiNO_3$-KNO_3(15.5:5:1)/H_2O, with the evaporation temperature varying from 5 °C to 15 °C. As shown in Figure 14a, the generation temperature decreased almost linearly with increasing the evaporation temperature. As shown in Figure 14b, the COP of the absorption refrigeration cycle increased with the evaporation temperature increasing, whereas the exergy efficiency decreased with the evaporation temperature increasing.
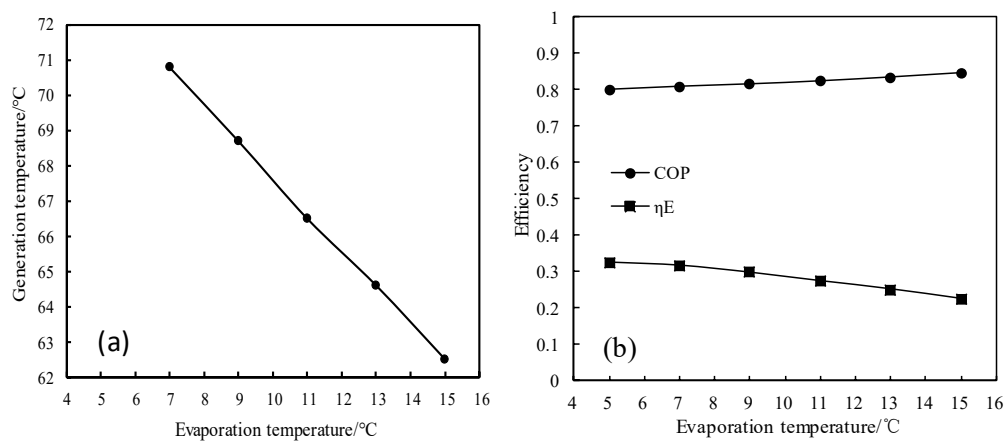
Figure 14. (**a**) Variation of the generation temperature with the evaporation temperature; and, (**b**) Variations of COP and η_E with the evaporation temperature.
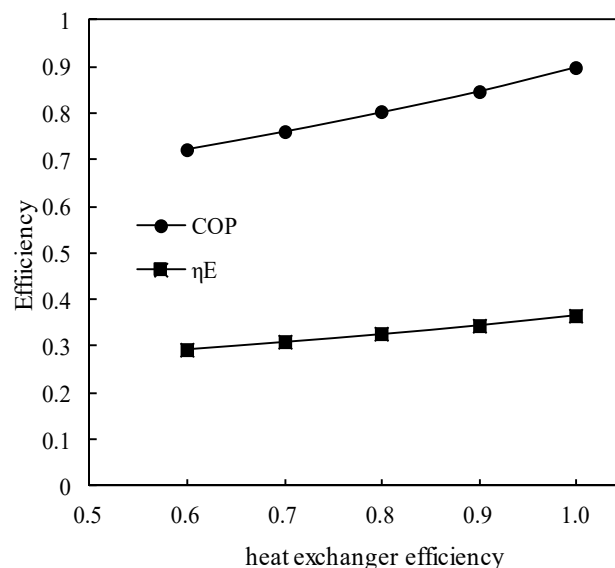
Figure 15. Variations of COP and η_E with the heat exchanger efficiency.

Figure 15 shows the variations of COP and η_E with the solution heat exchanger efficiency. COP and η_E increased almost linearly with the heat exchanger efficiency increasing, and the increasing slope of COP was greater than that of η_E.

3.10. Measurement of Corrosion Rate R_C

Generally, carbon steel is used as the structural material and copper is used as the heat exchange material for absorption heat pump. The R_C of carbon steel and copper in 63.5 wt.% solution of $CaCl_2$-$LiNO_3$-KNO_3(15.5:5:1)/H_2O were measured at 80.0 °C and pH 9.7. Figure 16 gives the comparison of R_C in 63.5 wt.% solution of $CaCl_2$-$LiNO_3$-KNO_3(15.5:5:1)/H_2O, 59.4 wt.% solution of $LiBr/H_2O$, and 60.3 wt.% solution of $CaCl_2$-$LiNO_3$-$LiBr$(8.72:1:1)/H_2O.
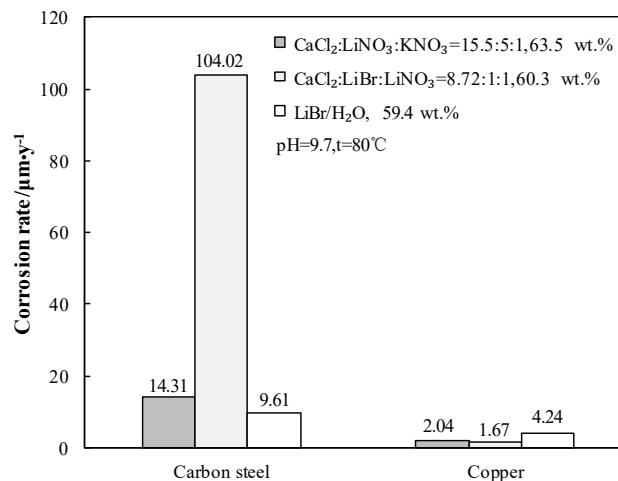
Figure 16. R_C of carbon steel and copper for $CaCl_2$-$LiNO_3$-KNO_3(15.5:5:1)/H_2O, $CaCl_2$-$LiNO_3$-$LiBr$(8.72:1:1) /H_2O and $LiBr/H_2O$.

Figure 16 shows that the R_c of carbon steel in 63.5 wt.% solution of $CaCl_2$-$LiNO_3$-KNO_3(15.5:5:1)/H_2O was 14.31 $\mu m \cdot y^{-1}$. Although the corrosivity of $CaCl_2$-$LiNO_3$-KNO_3(15.5:5:1)/H_2O to carbon steel was stronger than that of $LiBr/H_2O$, it was still acceptable for practical applications. On the other hand, the corrosivity of $CaCl_2$-$LiNO_3$-$LiBr$(8.72:1:1)/H_2O to carbon steel was too strong to be applied, even though it had the lowest generation temperature among the $CaCl_2$-based working pairs. The R_c of copper in 63.5 wt.% solution of $CaCl_2$-$LiNO_3$-KNO_3(15.5:5:1)/H_2O was 2.04 $\mu m \cdot y^{-1}$, which was smaller than that in 59.4 wt.% solution of $LiBr/H_2O$ and it could meet the requirements for engineering applications.

4. Conclusions

1. When compared with $LiBr/H_2O$, for an identical adsorption temperature at 0.872 kPa, which is a typical pressure of absorber, $CaCl_2/H_2O$ had a lower absorption temperature at 6.290 kPa, which is a typical pressure of generator, meaning that $CaCl_2/H_2O$ basically had a better refrigeration characteristic for an absorption refrigeration cycle. However, the absorption ability of $CaCl_2/H_2O$ was not strong enough for achieving an evaporation temperature of 5 °C or lower, because of its high crystallization temperature.
2. The crystallization temperature was significantly lowered when combining $CaCl_2/H_2O$ with $LiNO_3$ or $LiNO_3$+KNO_3. As a result, the absorption ability of $CaCl_2$-$LiNO_3/H_2O$ or $CaCl_2$-$LiNO_3$-KNO_3/H_2O was essentially improved.
3. For an absorption refrigeration cycle using $CaCl_2$-$LiNO_3$-KNO_3(15.5:5:1)/H_2O as the working pair, the generation temperature that is required for achieving an evaporation temperature of 5 °C was 74.0 °C, which was 7.0 °C lower than that using $LiBr/H_2O$.
4. When compared with $LiBr/H_2O$ under the same conditions, COP and η_E of the absorption refrigeration cycle with $CaCl_2$-$LiNO_3$-KNO_3(15.5:5:1)/H_2O were improved by 0.04 and 0.06, respectively.

5. R_C of carbon steel and copper in 63.5 wt.% solution of CaCl$_2$-LiNO$_3$-KNO$_3$(15.5:5:1)/H$_2$O at 80.0 °C and pH 9.7 were 14.31 and 2.04 μm·y^{-1}, respectively, which indicated that the corrosivity of the proposed working pair could meet the requirements for practical applications.

Author Contributions: Writing—Original Draft preparation, Y.L.; data curation, N.L.; methodology, C.L.; Writing—Review and Editing, Q.S.

Conflicts of Interest: The authors declare no conflict of interest.

Nomenclature

T	temperature, °C
w	mass concentration, %
T_C	crystallization temperature, °C
p	saturated vapor pressure, kPa
ρ	density, g·cm^{-3}
η	dynamic viscosity, mPa·s
C_p	specific heat capacity, kJ·kg^{-1}·K^{-1}
ΔH_{mix}	dissolution enthalpy, kJ·kg^{-1}
h	specific enthalpy, kJ·kg^{-1}
s	specific entropy, kJ·kg^{-1}·K^{-1}
AARD	average absolute relative deviation
a	circulation ratio
COP	coefficient of performance
E	exergy
ΔE	exergy destrction
η_E	exergy efficiency
R_C	corrosion rate, μm·y^{-1}

References

1. Srikhirin, P.; Aphornratana, S.; Chungpaibulpatana, S. A review of absorption refrigeration technologies. *Renew. Sustain. Energy Rev.* **2001**, *5*, 343–372. [CrossRef]
2. Wang, C. Application and development of absorption refrigeration technology. *Energy Technol.* **2000**, *21*, 31–35.
3. Hong, D.; Tang, L.; He, Y. A novel absorption refrigeration cycle. *Appl. Therm. Eng.* **2010**, *30*, 2045–2050. [CrossRef]
4. Abed, A.M.; Alghoul, M.A.; Sopian, K.; Majdi, H.S.; Al-Shamani, A.N.; Muftah, A.F. Enhancement aspects of single stage absorption cooling cycle: A detailed review. *Renew. Sustain. Energy Rev.* **2017**, *77*, 1010–1045. [CrossRef]
5. Bellos, E.; Tzivanidis, C.; Antonopoulos, K.A. Exergetic, energetic and financial evaluation of a solar driven absorption cooling system with various collector types. *Appl. Therm. Eng.* **2016**, *102*, 749–759. [CrossRef]
6. Leonzio, G. Solar systems integrated with absorption heat pumps and thermal energy storages: State of art. *Renew. Sustain. Energy Rev.* **2017**, *70*, 492–505. [CrossRef]
7. Alobaid, M.; Hughes, B.; Calautit, J.K.; O'Connor, D.; Heyes, A. A review of solar driven absorption cooling with photovoltaic thermal systems. *Renew. Sustain. Energy Rev.* **2017**, *76*, 728–742. [CrossRef]
8. Mehrabian, M.A.; Shahbeik, A.E. Thermodynamic modelling of a single-effect LiBr-H$_2$O absorption refrigeration cycle. *Proc. Inst. Mech. Eng. Part E-J. Process Mech. Eng.* **2005**, *219*, 261–273. [CrossRef]
9. Izquierdo, M.; Lizarte, R.; Marcos, J.D.; Gutiérrez, G. Air conditioning using an air-cooled single effect lithium bromide absorption chiller: Results of a trial conducted in Madrid in August 2005. *Appl. Therm. Eng.* **2008**, *28*, 1074–1081. [CrossRef]
10. Kaushik, S.C.; Arora, A. Energy and exergy analysis of single effect and series flow double effect water–lithium bromide absorption refrigeration systems. *Int. J. Refrig.* **2009**, *32*, 1247–1258. [CrossRef]

11. Sumathy, K.; Huang, Z.; Li, Z. Solar absorption cooling with low grade heat source—A strategy of development in South China. *Sol. Energy* **2002**, *72*, 155–165. [CrossRef]

12. Li, Z.; Jing, Y.; Liu, J. Thermodynamic study of a novel solar LiBr/H$_2$O absorption chiller. *Energy Build.* **2016**, *133*, 565–576. [CrossRef]

13. Sun, J.; Fu, L.; Zhang, S. A review of working fluids of absorption cycles. *Renew. Sustain. Energy Rev.* **2012**, *16*, 1899–1906. [CrossRef]

14. N'tsoukpoe, K.E.; Perier-Muzet, M.; Le-ierrès, N.; Luo, L.; Mangin, D. Thermodynamic study of a LiBr–H$_2$O absorption process for solar heat storage with crystallisation of the solution. *Sol. Energy* **2014**, *104*, 2–15. [CrossRef]

15. Xu, Z.; Wang, R.; Wang, H. Experimental evaluation of a variable effect LiBr-water absorption chiller designed for high-efficient solar cooling system. *Int. J. Refrig.* **2015**, *59*, 135–143. [CrossRef]

16. Lin, P.; Wang, R.; Xia, Z. Numerical investigation of a two-stage air-cooled absorption refrigeration system for solar cooling: Cycle analysis and absorption cooling performances. *Renew. Energy* **2011**, *36*, 1401–1412. [CrossRef]

17. Malinina, O.S.; Baranenko, A.V.; Zaitsev, A.V. Influence of the average daily outdoor air parameters on the efficiency of solar lithium bromide-water absorption refrigeration machine. In *AIP Conference Proceedings*; AIP Publishing: Melville, NY, USA, 2018; Volume 2007, p. 030040.

18. Mortazavi, M.; Schmid, M.; Moghaddam, S. Compact and efficient generator for low grade solar and waste heat driven absorption systems. *Appl. Energy* **2017**, *198*, 173–179. [CrossRef]

19. Bourouis, M.; Vallès, M.; Medrano, M.; Coronas, A. Performance of air-cooled absorption air-conditioning systems working with water-(LiBr+ LiI+ LiNO$_3$+ LiCl). *Part E J. Process Mech. Eng.* **2005**, *219*, 205–213. [CrossRef]

20. Jian, S.; Lin, F.; Shigang, Z. Performance calculation of single effect absorption heat pump using LiBr+ LiNO$_3$+ H$_2$O as working fluid. *Appl. Therm. Eng.* **2010**, *30*, 2680–2684. [CrossRef]

21. Chen, W.; Bai, Y. Thermal performance of an absorption-refrigeration system with [emim] Cu$_2$Cl$_5$/NH$_3$ as working fluid. *Energy* **2016**, *112*, 332–341. [CrossRef]

22. Bellos, E.; Tzivanidis, C.; Antonopoulos, K.A. Exergetic and energetic comparison of LiCl-H$_2$O and LiBr-H$_2$O working pairs in a solar absorption cooling system. *Energy Convers. Manag.* **2016**, *123*, 453–461. [CrossRef]

23. Wang, M.; Ferreira, C.A.I. Absorption heat pump cycles with NH$_3$–ionic liquid working pairs. *Appl. Energy* **2017**, *204*, 819–830. [CrossRef]

24. Luo, C.; Chen, K.; Li, Y.; Su, Q. Crystallization Temperature, Vapor Pressure, Density, Viscosity, and Specific Heat Capacity of the LiNO$_3$/[BMIM]Cl/H$_2$O Ternary System. *J. Chem. Eng. Data* **2017**, *62*, 3043–3052. [CrossRef]

25. Luo, C.; Li, Y.; Chen, K.; Li, N.; Su, Q. Thermodynamic properties and corrosivity of a new absorption heat pump working pair: Lithium nitrate+ 1-butyl-3-methylimidazolium bromide+ water. *Fluid Phase Equilib.* **2017**, *451*, 25–39. [CrossRef]

26. Luo, C.; Li, Y.; Li, N.; Wang, Y.; Su, Q. Thermophysical properties of lithium nitrate+ 1-ethyl-3-methylimidazolium diethylphosphate+ water system. *J. Chem. Thermodyn.* **2018**, *126*, 160–170. [CrossRef]

27. Luo, C.; Wang, Y.; Li, Y.; Wu, Y.; Su, Q.; Hu, T. Thermodynamic properties and application of LiNO$_3$-[MMIM][DMP]/H$_2$O ternary working pair. *Renew. Energy* **2019**, *134*, 147–160. [CrossRef]

28. Luo, C.; Li, Y.; Li, N.; Su, Q. Thermodynamic properties and evaluation of the lithium nitrate–imidazole IL–water ternary systems as new working fluids for a double-effect AHP cycle. *Int. J. Refrig.* **2018**, *90*, 58–72. [CrossRef]

29. Li, N.; Luo, C.; Su, Q. A working pair of CaCl$_2$–LiBr–LiNO$_3$/H$_2$O and its application in a single-stage solar-driven absorption refrigeration cycle. *Int. J. Refrig.* **2018**, *86*, 1–13. [CrossRef]

30. Li, N.; Luo, C.; Su, Q. Thermophysical properties and corrosivity of CaCl$_2$-LiBr-LiNO$_3$-KNO$_3$/H$_2$O working pair. *Chin. J. Process Eng.* **2018**, *18*, 764–768.

31. Li, N.; Luo, C.; Su, Q. Thermophysical properties and applications of CaCl$_2$-LiBr(1.35:1)/H$_2$O as a working pair. *Chin. J. Eng.* **2018**, *40*, 167–176.

32. Li, N.; Li, Y.; Luo, C.; Su, Q. Thermophysical properties and applications of CaCl$_2$-LiNO$_3$/H$_2$O ternary working pair. *Chem. Ind. Eng. Prog.* **2018**, *37*, 4625–4637.

33. Park, Y.; Kim, J.S.; Lee, H.; Yu, S.I. Density, vapor pressure, solubility, and viscosity for water+ lithium bromide+ lithium nitrate+ 1, 3-propanediol. *J. Chem. Eng. Data* **1997**, *42*, 145–148. [CrossRef]

34. Safarov, J.T. Vapor pressure of heat transfer fluids of absorption refrigeration machines and heat pumps: Binary solutions of lithium nitrate with methanol. *J. Chem. Thermodyn.* **2005**, *37*, 1261–1267. [CrossRef]

35. Verevkin, S.; Safarov, J.; Bich, E.; Hassel, E.; Heintz, A. Study of vapour pressure of lithium nitrate solutions in ethanol. *J. Chem. Thermodyn.* **2006**, *38*, 611–616. [CrossRef]

36. Gao, Q.; Zheng, D.; Jiang, C. Thermodynamic study on the working of HEAT–TYPE absorption heat pump. *Petrochem. Technol.* **1993**, *22*, 382–392.

37. Chen, D.; Xie, J. *Technology and Application of Heat Pump*; Chemical Industry Press: Beijing, China, 2006; pp. 206–220.

38. Yang, D.; Zhu, Y.; Liu, S.; Lv, H.; Luo, C. Thermodynamic Properties of a Ternary AHP Working Pair: Lithium Bromide+ 1-Ethyl-3-methylimidazolium Chloride+ H_2O. *J. Chem. Eng. Data* **2019**, *64*, 574–583. [CrossRef]

39. Aprhornratana, S.; Eames, I.W. Thermodynamic analysis of absorption refrigeration cycles using the second law of thermodynamics method. *Int. J. Refrig.* **1995**, *18*, 244–252. [CrossRef]